Applied Catalysis B: Environmental 337 (2023) 123010

Contents lists available at ScienceDirect

Applied Catalysis B: Environmental

journal homepage: www.elsevier.com/locate/apcatb

Coke-resistant $NdFe_{0.7}Ni_{0.3}O_3$ perovskite catalyst with superior stability for dry reforming of ethane

Yaning Wang [a], Xiaohang Sun [a], Xiaohan Yu [a], Rongjun Zhang [b], Binhang Yan [a,*]

[a] Department of Chemical Engineering, Tsinghua University, Beijing 100084, China
[b] Research Institute of Petroleum Processing, SINOPEC, Bejing 100083, China

ARTICLE INFO

Keywords:
Dry reforming
Perovskite
Oxygen vacancy
Coke resistance
CO_2 activation

ABSTRACT

Effects of A-site cation substitution and B-site active metal doping-segregation on physicochemical properties of Ni-doped perovskite-structured $LnFe_{0.7}Ni_{0.3}O_3$ (Ln = La, Nd, Sm, Eu) catalysts and their catalytic performance for dry reforming of ethane (DRE) were studied. The DRE activity follows the trend: $NdFe_{0.7}Ni_{0.3}O_3$ > $SmFe_{0.7}Ni_{0.3}O_3$ > $EuFe_{0.7}Ni_{0.3}O_3$ > $LaFe_{0.7}Ni_{0.3}O_3$. The doping-segregation process of Ni was demonstrated by in-situ X-ray Diffraction (XRD) and X-ray Absorption Fine Structure (XAFS) measurements, which significantly improves the dispersion of Ni and enhance the interaction between metal and support. The results of temperature-programmed surface reactions (TPSR) and pulse reactions indicate that oxygen vacancies generated by the exsolution of Ni play an important role in the elimination of coke and shift the product from surface carbon to gaseous CO. According to the in-situ Raman experiments, the superior catalytic stability (no coke deposition or activity loss over 100 h) of $NdFe_{0.7}Ni_{0.3}O_3$ is ascribed to its strong resistance towards carbon deposition.

1. Introduction

Hydrogen is one of the most important materials for the chemical and petrochemical industry, such as ammonia synthesis, methanol synthesis, Fischer-Tropsch synthesis, and petroleum refining processes [1,2]. Hydrogen can be produced from various sources such as coal gasification [3], water electrolysis [4], and steam or dry reforming of organic compounds [5]. The recent discovery of abundant shale gas reserves offers a possibility of catalytic conversion of light alkanes (especially methane and ethane) from shale gas to hydrogen through dry reforming reactions [6,7]. Dry reforming of light alkanes not only produces an industrially important synthesis gas but also reduces CO_2 emission. In recent years, dry reforming of methane (DRM) has been extensively investigated as a promising process to consume CO_2 and produce syngas. However, the DRM process is highly endothermic and should be performed at high temperatures, leading to severe coke deposition and metal sintering. An alternative way for DRM is dry reforming of ethane (DRE, Eq. (1)), which could potentially decrease the operating temperature and reduce the cost. As the thermodynamic calculation results shown in Fig. S1, CO_2 reaches 100 % conversion at ~973 K for DRE, which is 200 K lower than DRM.

$$C_2H_6 + 2CO_2 \rightarrow 4CO + 3H_2 \quad \Delta H^0_{298K} = 428\ kJ/mol \tag{1}$$

Commonly, Ni-based catalysts have been widely used for CO_2 reforming of light alkanes with the advantages of considerable catalytic activity, readily available stocks, and lower cost compared to precious metal catalysts [8]. However, carbon deposition during reaction is one of the most challenging aspects currently confronted for Ni-based catalysts. The resulting carbonaceous materials are built up on the surface of the catalyst, causing it to lose activity and subsequently stalling the overall process. To solve the problem of the instability of Ni-based catalysts, structured catalysts have particular potential for catalytic applications at high temperatures due to their well-dispersed active phase and high thermal stability [9]. Perovskites with the ideal general formula of ABO_3 are known as versatile materials that allow different cations to be incorporated into their structures [10–12]. The reversible incorporation of transition-metal catalysts into perovskite lattices has been receiving an increasing amount of attention for heterogeneous catalysts [13–15]. The transition metal ions at B-site are generally believed to be active for catalysis because they can interact with gas molecules (reactants and intermediates) through a set of *d* orbitals [16]. It is acknowledged that the B-site partial substitution of Fe in $LaNiO_3$ can stabilize the perovskite structure so that the $LaFe_xNi_{1-x}O_3$ perovskite

* Corresponding author.
E-mail address: binhangyan@tsinghua.edu.cn (B. Yan).

https://doi.org/10.1016/j.apcatb.2023.123010
Received 4 January 2023; Received in revised form 23 April 2023; Accepted 16 June 2023
Available online 17 June 2023

structure survives during the DRM reaction and stabilizes the long-term performance by providing stronger metal-support interaction [17,18].

The role of rare-earth cations at A-site is considered to be less decisive as long as they are trivalent. However, it is confirmed that the substitution at A-site may remarkably enhance the catalytic activity of perovskites by modifying the electronic state of B-site cations and/or introducing oxygen vacancies [19]. Moradi et al. [20] investigated the influence of partial substitution of alkaline earth metals namely Mg, Sr, and Ba, with La in the $La_{1-x}M_xNiO_3$ perovskite catalyst and tested their application in DRM reaction. Choi et al. [21] reported that Ce-substitution in $LaFe_{0.7}Ni_{0.3}O_3$ enhanced the catalytic activity towards steam reforming of methane. Wang et al. [22] proposed that the Ce^{3+} cation at the A-site of $(LaCe)(NiFe)O_3$ improved the catalytic activity of the perovskite by introducing more oxygen vacancies.

However, there still remains a gap in understanding the role A site cations play in the catalytic performance of perovskites. In the present work, dry reforming of ethane was carried out over $LnFe_{0.7}Ni_{0.3}O_3$ (Ln = La, Sm, Eu, Nd) perovskite and the supported $Ni/LnFeO_3$ catalysts. The physical and chemical properties of the catalysts were characterized by various techniques, such as X-ray photoelectron spectroscopy (XPS) and X-ray absorption spectroscopy (XAS). Moreover, temperature-programmed surface reactions (TPSR) were carried out to investigate the ability of catalysts for CO_2 and C_2H_6 activation. In-situ Raman spectra were collected to monitor the formation and oxidation of carbon species on the catalysts. Pulse reaction studies and step response reactions were conducted to explore the effect of oxygen vacancies on the mechanism for ethane activation and coking resistance.

2. Experimental

2.1. Catalyst synthesis

Mixed-oxide catalyst precursors $LnFe_{0.7}Ni_{0.3}O_3$ (Ln = La, Sm, Eu, Nd) were prepared by a sol-gel self-combustion method, in which citric acid ($C_6H_8O_7{\cdot}H_2O$) was used as complexing agent [23]. The starting materials were $Ln(NO_3)_3{\cdot}xH_2O$ (99.5 %), $Ni(NO_3)_2{\cdot}6H_2O$ (99 %), $Fe(NO_3)_3{\cdot}9H_2O$ (99 %), and $C_6H_8O_7{\cdot}H_2O$ (99.5 %), which were purchased from Aladdin Company. All the chemicals were of analytical grade and used directly without any further purification. $Ln(NO_3)_3{\cdot}xH_2O$, $Ni(NO_3)_2{\cdot}6H_2O$, $Fe(NO_3)_3{\cdot}9H_2O$ were dissolved in distilled water and $C_6H_8O_7{\cdot}H_2O$ was added under constant stirring successively. The molar ratio between $C_6H_8O_7{\cdot}H_2O$ and the total metal ions (Ln^{3+}, Ni^{2+}, and Fe^{3+}) was set as 1.5:1. After stirring for 6 h at 363 K, the solution was heated on a heating plate until it ignited. The obtained powder in the spongy form was collected and calcined in air at 1023 K for 3 h.

The reference catalysts $Ni/LnFeO_3$ were prepared by the wetness impregnation method. The $LnFeO_3$ support was synthesized using the same procedure as mentioned above for perovskite synthesis. $Ni(NO_3)_2{\cdot}6H_2O$ were impregnated onto the support with excess water. The Ni content for all Ni-contained catalysts was 7.2 wt%. After being dried at 383 K overnight, the supported catalysts were calcined at 873 K for 3 h.

2.2. Catalyst characterization

The synthesized catalysts were characterized by both ex-situ and in-situ X-ray diffraction (XRD). As for the ex-situ XRD, the diffraction patterns were collected with 2θ values from 10° to 80° using a XRD diffractometer (Rigaku MiniFlex 600, Japan) equipped with a Cu Kα source. A Bruker D8 ADVANCE Diffractometer with Cu Kα (45 kV, 50 mA) equipped with a reaction cell was used for the in-situ XRD measurements. 20 mL/min 5 % H_2/Ar was introduced to the reaction cell and the temperature was increased from 303 to 873 K at a rate of 10 K/min.

X-ray photoelectron spectroscopy (XPS) experiments were carried out in a SPECS instrument (Thermo Fisher ESCALAB 250Xi) under ultrahigh vacuum (1.33×10^{-8} Pa) conditions at a pass energy of 30 eV. Non-monochromatic Al Kα radiation (1486.6 eV) was used to provoke electron emission from the samples. The catalyst was mounted onto the sample holder and the chamber was degassed to the required vacuum conditions. The binding energies (BE) of the different elements were calibrated internally using the BE of carbon C1s at 284.8 eV.

Specific surface area of the catalysts was measured by N_2 adsorption-desorption isotherm at 77 K with a Quantachrome autosorbiQ and AsiQwin instrument using Brunauer-Emmett-Teller (BET) model. Prior to the measurements, the samples were degassed under vacuum at 393 K for 2 h to remove any moisture and impurities adsorbed on the catalysts.

CO pulse chemisorption was conducted to determine the dispersion of Ni on the surface of the catalysts. Before chemisorption, the samples were reduced with 25 mL/min 20 % H_2/Ar at 873 K for 1 h. After reduction, the samples were heated to 883 K to desorb the adsorbed H_2 in Ar and then cooled down to 293 K. After pretreatment, the samples were injected with 10 % CO/Ar until the surface of the active metal is saturated with chemisorbed CO.

The quantity of carbon formed during dry reforming was determined by Thermogravimetric analysis (TGA) of the used catalysts. The experiments were performed in a METTLER TOLEDO equipment (TGA/DSC1/1600). The weight change observed for the spent catalyst (10 mg) during heating under 50 mL/min air from room temperature to 1073 K (10 K/min) was measured.

X-ray absorption fine structure (XAFS) data were collected in the fluorescence mode at the beamline 4B9A of the Beijing Synchrotron Radiation Facility (BSRF). The normalization and the adsorption spectra were fitted by ATHENA (IFEFFIT 1.2.11 data analysis package) with the spectra of Ni foil (Ni^0) and NiO (Ni^{2+}) as references. Synchrotron soft X-ray absorption spectra (sXAS) were obtained at the beamline 4B9B of the BSRF, operated at an energy of 2.5 GeV with a maximum stored current of 250 mA.

Both ex-situ and in-situ Raman experiments were performed to characterize the nature of carbon formed in the DRE reaction. As for ex-situ Raman, the Raman spectra were recorded at room temperature using a Horiba LabRam HR evolution spectrometer, equipped with a He-Ne laser (λ = 532 nm) of 10 mW power, a CCD detector, and an Olympus microscope with an objective lens of 50×. In-situ Raman measurements were carried out by using a homemade optical Raman cell. The samples were pretreated in 25 mL/min 20 % H_2/Ar at 873 K for 1 h. Following the reduction, the gas was switched to 20 mL/min 20 % C_2H_6/Ar, 20 % CO_2/Ar, and 20 % O_2/Ar successively. In-situ Raman spectra with two accumulations of 30 s each were obtained under different atmospheres.

Diffuse reflectance infrared Fourier transform spectroscopy (DRIFTS) with CO as a probe molecule was performed using an FTIR spectrometer (Thermo Scientific Nicolet iS50). Approximately 20 mg of fine catalyst powder was packed into the homemade DRIFTS cell and the surface was smoothly flattened to enhance IR reflection. The catalyst was first reduced at 873 K for 60 min in a 20 mL/min 25 % H_2/Ar flow. After cooling down to 293 K, background spectra of 64 scans with a resolution of 4 cm^{-1} were recorded. The 10 % CO/Ar mixture with a total flow rate of 20 mL/min was introduced into the cell for 10 min and then the sample spectra (64 scans) were again collected.

2.3. Flow reactor studies

Dry reforming reaction was performed under atmospheric pressure in a fixed-bed tubular quartz reactor. The catalyst grains (40 mg) were kept in place using quartz wool plugs. The temperature of the reactor was measured by a thermocouple located inside on top of the catalyst bed. All catalysts were reduced with a 25 % H_2/N_2 flow (20 mL/min) at 873 K for 1 h. Following reduction, a feed gas mixture containing C_2H_6: CO_2: N_2 in a ratio of 1:2:1 with a rate of 40 mL/min was introduced.

The reaction products were analyzed online using a gas chromatography (GC, Agilent 7890B), equipped with a flame ionization de-

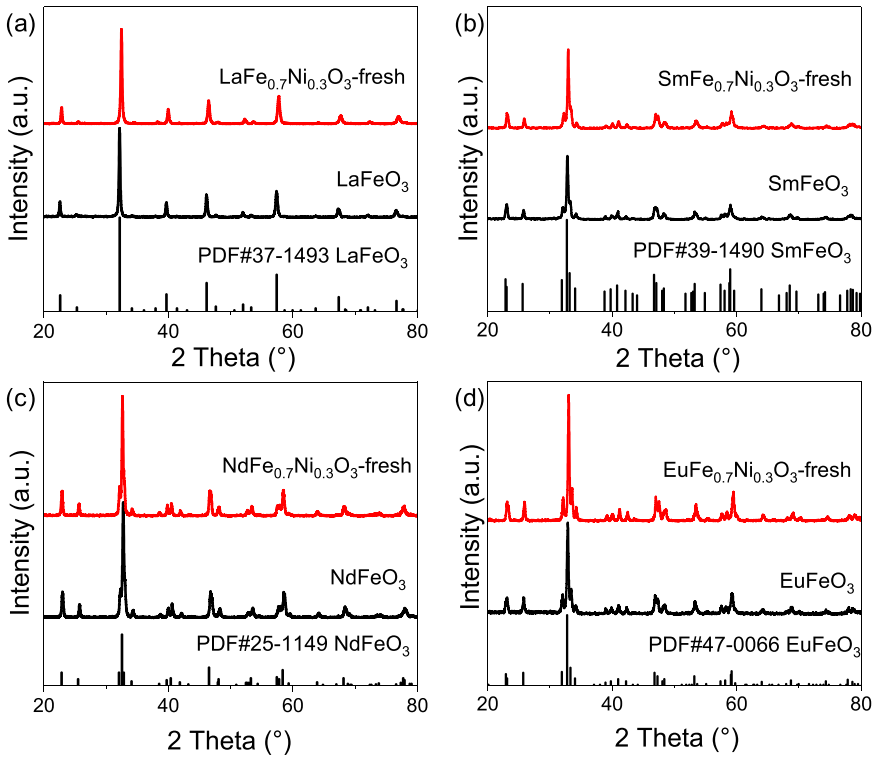

Fig. 1. X-ray diffraction (XRD) patterns of fresh $LnFe_{0.7}Ni_{0.3}O_3$ (Ln =La, Sm, Eu, Nd) and $LnFeO_3$ perovskite catalysts: (a) $LaFe_{0.7}Ni_{0.3}O_3$ and $LaFeO_3$, (b) $SmFe_{0.7}Ni_{0.3}O_3$ and $SmFeO_3$, (c) $NdFe_{0.7}Ni_{0.3}O_3$ and $NdFeO_3$, (d) $Eu_{0.7}Ni_{0.3}O_3$ and $EuFeO_3$.

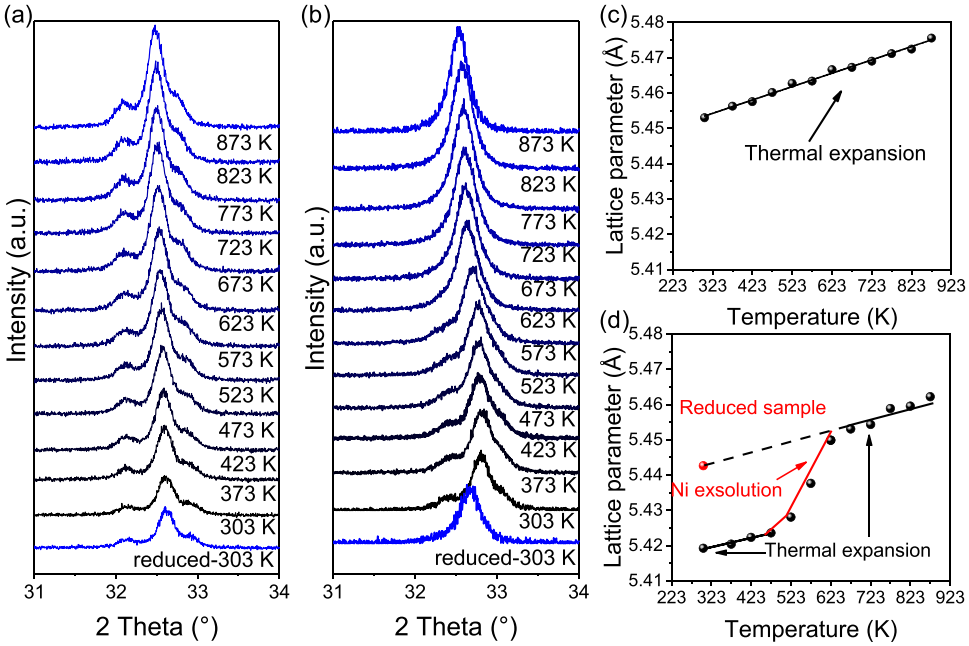

Fig. 2. XRD patterns of catalysts during reductive heating in the temperature range of 303–873 K: (a) $Ni/NdFeO_3$ and (b) $NdFe_{0.7}Ni_{0.3}O_3$; Evolution of the lattice parameter of perovskite structure for the catalysts: (c) $Ni/NdFeO_3$ and (d) $NdFe_{0.7}Ni_{0.3}O_3$. The lattice constant was calculated from the position of (121) plane reflection.

tector (FID) and a thermal conductivity detector (TCD), in the presence of carrier gas, argon. A blank quartz reactor was used to perform the control experiments at 873 K, which showed negligible activity and indicated that gas-phase reactions and quartz do not contribute to the catalytic activity. The catalytic properties were evaluated in terms of reactant conversion and turnover frequency (TOF) as follows:

$$X_{\text{reactant}} = \frac{F^{\text{inlet}}_{\text{reactant}} - F^{\text{outlet}}_{\text{reactant}}}{F^{\text{inlet}}_{\text{reactant}}} \times 100\ \% \tag{2}$$

$$\text{TOF} = \frac{F^{\text{inlet}}_{\text{reactant}} \times X}{U_{\text{CO}} \times W_{\text{catalyst}}},\ \text{s}^{-1} \tag{3}$$

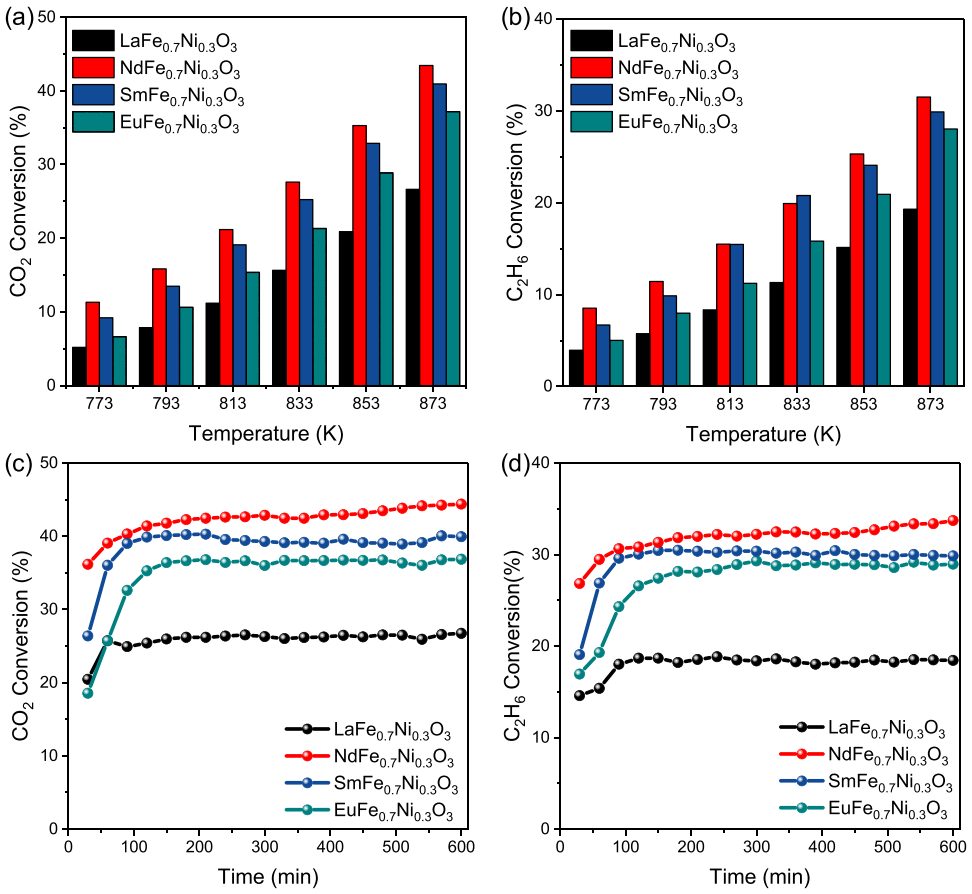

Fig. 3. Conversion of reactants over $LnFe_{0.7}Ni_{0.3}O_3$ in the temperature range of 773–873 K at 1 atm: (a) CO_2 and (b) C_2H_6; Conversion of reactants over $LnFe_{0.7}Ni_{0.3}O_3$ (Ln = La, Nd, Sm, Eu) during the steady-state reaction at 873 K: (c) CO_2 and (d) C_2H_6. Reaction conditions: 40 mg catalysts, 1 atm, $C_2H_6/CO_2/N_2$ = 1:2:1, and gas hourly space velocity (GHSV) = 60,000 mL/(h•g_{cat}).

Table 1
Results of the CO chemisorption and flow reactor studies. Values of conversion, yield, and TOF were calculated by averaging data points between 8 and 10 h on stream at 873 K and 1 atm.

Catalyst	Conversion (%)		E_a (kJ/mol)		Yield (%)		CO uptake (μmol g^{-1})	TOF (s^{-1})	
	CO_2	C_2H_6	CO_2	C_2H_6	CO	H_2		CO_2	C_2H_6
$LaFe_{0.7}Ni_{0.3}O_3$	26.6	19.3	97.9	94.8	18.8	11.8	30.7	1.6	1.2
$NdFe_{0.7}Ni_{0.3}O_3$	43.4	31.5	79.5	76.4	30.8	23.1	81.0	1.0	0.7
$SmFe_{0.7}Ni_{0.3}O_3$	41.0	29.9	84.3	83.8	29.4	18.7	31.9	2.4	1.7
$EuFe_{0.7}Ni_{0.3}O_3$	37.2	28.0	96.0	95.1	27.5	19.8	50.3	1.4	1.0
$Ni/LaFeO_3$	29.3	20.9	110.8	105.7	20.6	14.4	71.2	0.8	0.5
$Ni/NdFeO_3$	-	-	99.3	98.7	-	-	73.6	-	-

where F is the molar flow rate of the reactant, mol s^{-1}, U_{CO} is the CO uptake value determined by CO chemisorption, $mol_{CO}{\cdot}g^{-1}$; and $W_{catalyst}$ is the weight of catalyst used, g.

The selectivity (S) and yields (Y) were defined as Eqs. (4)–(10) based on the consumption of C_2H_6, and space-time yields (STY) were calculated by using Eqs. (11) and (12):

$$S_{CO} = \frac{F^{outlet}_{CO\ originated\ from\ C_2H_6}}{2 \times (F^{inlet}_{C_2H_6} - F^{outlet}_{C_2H_6})} \times 100\% \quad (4)$$

The amount of CO produced from C_2H_6 is calculated based on the oxygen balance as a part of CO is produced from CO_2:

$$F^{outlet}_{CO\ originated\ from\ C_2H_6} = F^{outlet}_{CO} - \left(\frac{F^{outlet}_{CO} + F^{outlet}_{H_2O}}{2}\right) \quad (5)$$

$$S_{CH_4} = \frac{F^{outlet}_{CH_4}}{2 \times (F^{inlet}_{C_2H_6} - F^{outlet}_{C_2H_6})} \times 100\% \quad (6)$$

$$S_{C_2H_4} = \frac{F^{outlet}_{C_2H_4}}{F^{inlet}_{C_2H_6} - F^{outlet}_{C_2H_6}} \times 100\% \quad (7)$$

$$S_{H_2} = \frac{F^{outlet}_{H_2}}{3 \times (F^{inlet}_{C_2H_6} - F^{outlet}_{C_2H_6})} \quad (8)$$

$$Y_{CO} = X_{C_2H_6} \times S_{CO} \quad (9)$$

$$Y_{H_2} = X_{C_2H_6} \times S_{H_2} \quad (10)$$

$$STY_{CO} = \frac{F^{outlet}_{CO}}{W_{catalyst}} \times \frac{3600\ s}{1\ h} \quad (11)$$

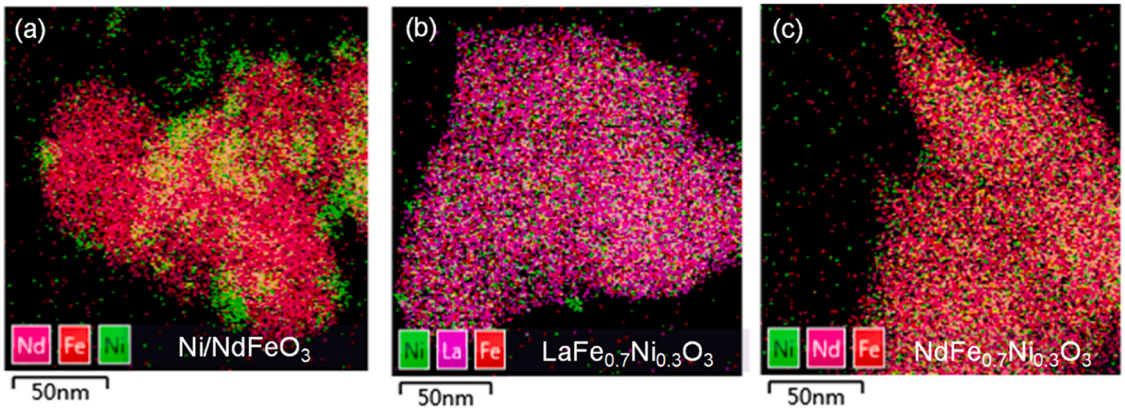

Fig. 4. Energy dispersive X-ray (EDX) elemental mapping of spent catalysts: (a) $Ni/NdFeO_3$, (b) $LaFe_{0.7}Ni_{0.3}O_3$, and (c) $NdFe_{0.7}Ni_{0.3}O_3$.

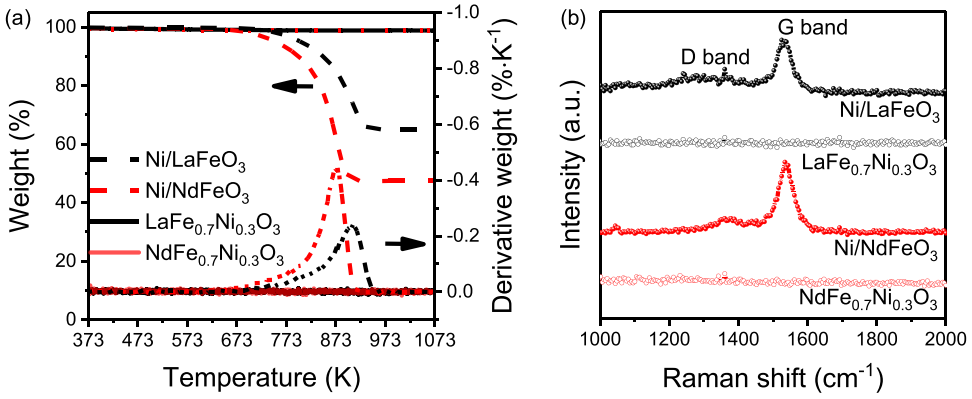

Fig. 5. Characterization of spent $LaFe_{0.7}Ni_{0.3}O_3$, $NdFe_{0.7}Ni_{0.3}O_3$, $Ni/LaFeO_3$, and $Ni/NdFeO_3$ catalysts: (a) thermogravimetry and derivative thermogravimetry and (b) Raman.

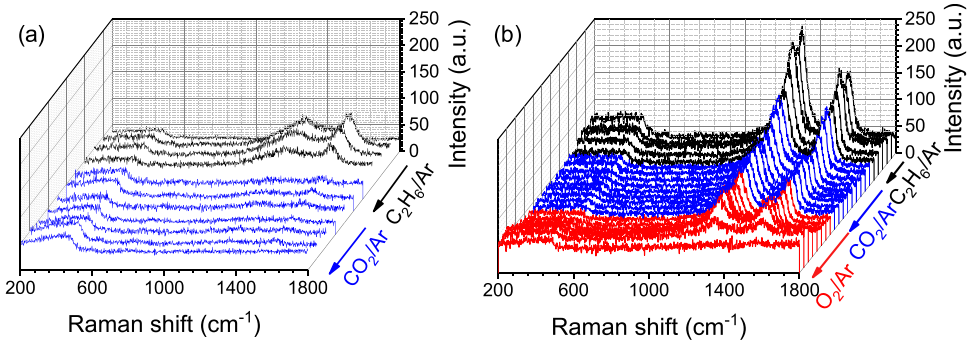

Fig. 6. In-situ Raman spectra of coke deposition on the catalysts under C_2H_6/Ar (black), CO_2/Ar (blue) and O_2/Ar (red) atmosphere: (a) $NdFe_{0.7}Ni_{0.3}O_3$ and (b) $Ni/NdFeO_3$. The band between 200 and 600 cm^{-1} is ascribed to the Raman signals of the optical quartz window of the homemade Raman cell.

$$STY_{H_2} = \frac{F_{H_2}^{outlet}}{W_{catalyst}} \times \frac{3600\ s}{1\ h} \quad (12)$$

2.4. Temperature-programmed surface reaction (TPSR) studies

During the H_2 temperature-programmed reduction (H_2-TPR) measurements, 20 mg of calcined sample was loaded into a quartz tube. The catalyst samples were degassed at 473 K for 1 h in a Ar flow to mitigate the physically adsorbed impurities followed by cooling to room temperature. For the H_2-TPR studies, the samples were heated from room temperature to 1073 K at 10 K/min in a 5 % H_2/Ar flow with a flow rate of 20 mL/min. A gas chromatography (Agilent 8860) with a TCD was positioned at the exit to monitor the consumption of H_2.

C_2H_6-TPSR and CO_2-TPSR over the perovskite catalysts were conducted to explore the ability for C_2H_6 and CO_2 activation, respectively. Prior to each experiment, the sample was pretreated in a 20 mL/min 20 % H_2/N_2 flow at 873 K for 1 h and cooled to room temperature followed by purging with N_2 for 1 h. Thereafter, the pretreated sample was exposed to 20 mL/min 20 % C_2H_6/N_2 or 20 % CO_2/N_2, and the temperature was increased to 1073 K at a rate of 10 K/min. The outlet gas was analyzed using an online FTIR spectrometer (Thermo Fisher Nicolet-iS50) equipped with a gas cell.

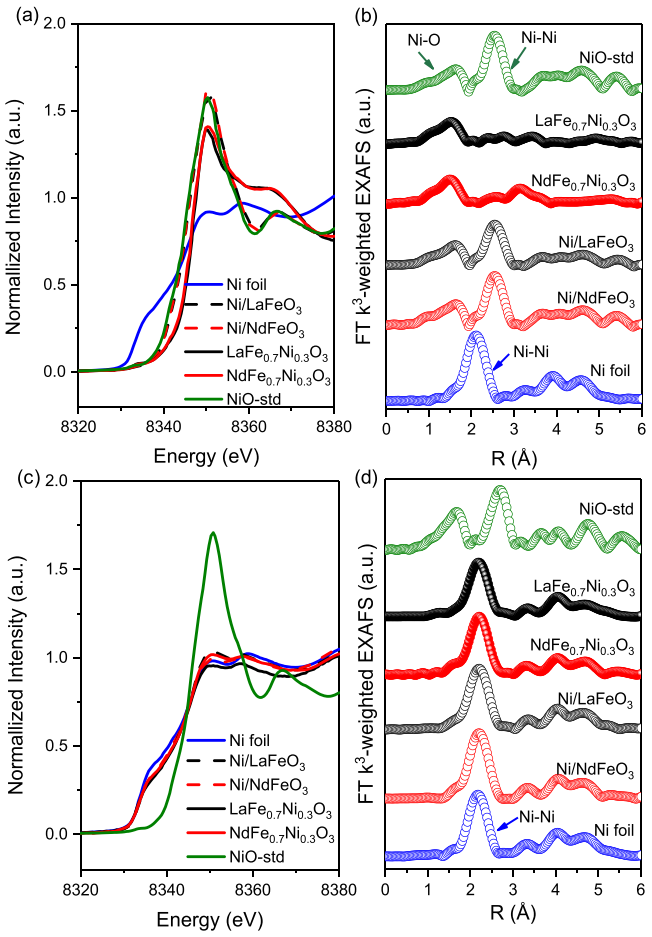

Fig. 7. Ni K-edge XAS results of pristine catalysts: (a) Normalized XANES spectra and (b) Fourier transformed k^3-weighted EXAFS data; Ni K-edge XAS results of spent catalysts: (c) Normalized XANES spectra and (d) Fourier transformed k^3-weighted EXAFS data.

2.5. Step response studies

Step response studies were carried out to investigate the transient kinetics of the DRE reaction over perovskite catalysts. A four-way valve was used to switch between Ar and C_2H_6/Ar. Before each reaction, the catalysts were pretreated at 873 K for 1 h in a 20 mL/min 20 % H_2/Ar flow. After the reactor was swept with Ar, the feed was switched to 10 mL/min C_2H_6. An online mass spectrometer was used to monitor the concentration responses.

2.6. Pulse reaction studies

Isothermal pulse experiments were performed at 873 K using a quartz tube reactor, which was filled with about 50 mg catalyst. The gas volume in a single pulse was controlled via a gas loop with a volume of 280 μL. The catalysts were reduced at 873 K for 1 h in a 20 mL/min 10 % H_2/ N_2 flow. Following the reduction, the reactor was purged with N_2 and then 15 pulses of 20 % CO_2/N_2 were introduced into the reactor. After CO_2 pulses, the reactor was purged with a N_2 flow for 30 min and then 10 pulses of 20 % C_2H_6/N_2 were admitted into the reactor. The gas phase products of each pulse were detected by a GC (Agilent 7890B).

3. Results and discussion

3.1. Synthesis of perovskite catalysts

XRD patterns of fresh $LnFe_{0.7}Ni_{0.3}O_3$ and $LnFeO_3$ (Ln = La, Sm, Eu, Nd) perovskite catalysts synthesized by the citrate sol-gel method were obtained and shown in Fig. 1. The XRD patterns suggest the formation of perovskite phase for $LnFeO_3$ catalysts. The successful doping and exsolution of Ni in the perovskite lattice are confirmed by ex-situ XRD results shown in Fig. S2. After Ni doping, the XRD patterns of the perovskite phase of $LnFe_{0.7}Ni_{0.3}O_3$ catalysts shift towards higher 2θ values as the radius of Ni^{3+} (0.56 Å) is smaller than that of Fe^{3+} (0.65 Å). The results indicate the incorporation of Ni^{3+} and the formation of a new perovskite phase.

In-situ XRD experiments were also carried out to investigate the change in the lattice structure of the catalysts under different temperatures at a reducing atmosphere. As displayed in Fig. 2(a) and (b), the shift of the diffraction peaks to lower angles as the increase of temperature is observed on both $NdFe_{0.7}Ni_{0.3}O_3$ and $Ni/NdFeO_3$. The lattice parameter of $Ni/NdFeO_3$ experiences a linear increase in the temperature range of 303–873 K, which is ascribed to the thermal expansion of the lattice. However, an abrupt change is observed over $NdFe_{0.7}Ni_{0.3}O_3$ at 423–623 K, demonstrating the expulsion of Ni dopant atoms from the lattice of $NdFeO_3$.

The reduction properties of Ni-substituted perovskites were further investigated by H_2-TPR. As displayed in Fig. S3, $Ni/NdFeO_3$ and $Ni/LaFeO_3$ exhibit two peaks, which are ascribed to the reduction of Ni^{2+} to metallic Ni and the partial reduction of Fe^{3+}. While another peak at a lower temperature is observed over $NdFe_{0.7}Ni_{0.3}O_3$ and $LaFe_{0.7}Ni_{0.3}O_3$, which is due to the reduction of Ni^{3+} to Ni^{2+} in the perovskite. Compared to La^{3+} as an A-site cation, the shift of the reduction peak of Ni^{2+} to higher temperature is observed over $Ni/NdFeO_3$ and $NdFe_{0.7}Ni_{0.3}O_3$, suggesting a stronger interaction between Ni and $NdFeO_3$. Combined with the in-situ XRD results, it is suggested that the Ni ions can be reduced to metallic Ni at the reforming temperature of 873 K for the $NdFe_{0.7}Ni_{0.3}O_3$ and $LaFe_{0.7}Ni_{0.3}O_3$ catalysts.

The EDX elemental mapping images of reduced catalysts are shown in Fig. S4. It can be seen from EDX results that the A-site cations and Fe ions are homogeneously distributed in the catalysts. Agglomerated Ni particles are observed over $Ni/LaFeO_3$ and $Ni/NdFeO_3$ while Ni species are uniformly dispersed over $NdFe_{0.7}Ni_{0.3}O_3$ and $LaFe_{0.7}Ni_{0.3}O_3$ catalysts. The increase in Ni dispersion would provide more active sites for the activation of ethane, which is beneficial to the enhancement of DRE activity.

3.2. Performance of perovskite catalysts

The influence of the reaction temperature on the conversion of CO_2 and C_2H_6 is depicted in Fig. 3(a) and (b). The experimental data indicate that the A-site cations in perovskite play an important role in the DRE activity. It can be seen that the catalytic activity follows the trend: $NdFe_{0.7}Ni_{0.3}O_3 > SmFe_{0.7}Ni_{0.3}O_3 > EuFe_{0.7}Ni_{0.3}O_3 > LaFe_{0.7}Ni_{0.3}O_3$. As shown in Table S1, CO, C_2H_4 and CH_4 were the main carbon-containing products, representing dry reforming, dehydrogenation and cracking of C_2H_6, respectively [24]. Over 97 % CO selectivity indicates that most ethane is converted into CO rather than C_2H_4 since the scission of the C-C bond is much easier than the scission of C-H bonds over Ni. The steady-state catalytic performance at 873 K is displayed in Fig. 3(c) and (d), the conversion of CO_2 and C_2H_6 maintains steady over the Ni-doped $LnFe_{0.7}Ni_{0.3}O_3$ catalysts after 10 h reaction. A slight increase in the conversion is due to the consecutive exsolution of Ni from the perovskite lattice. The BET specific surface areas listed in Table S2 show no obvious correlation between the catalytic performance with the surface area of catalysts. As a reference, the flow reactor experiments of DRE were also carried out over $Ni/LaFeO_3$ and $Ni/NdFeO_3$, and the results are displayed in Fig. S5. For $Ni/NdFeO_3$, the reactor was blocked severely so that the gas could not flow through the catalyst bed. In contrast, the $LnFe_{0.7}Ni_{0.3}O_3$ catalysts exhibit better performance in both activity and stability. As displayed in Table 1, the catalysts exhibit relatively similar TOF. However, the TOF calculated based on Ni atoms may not be accurate enough since CO adsorption strength is different over the

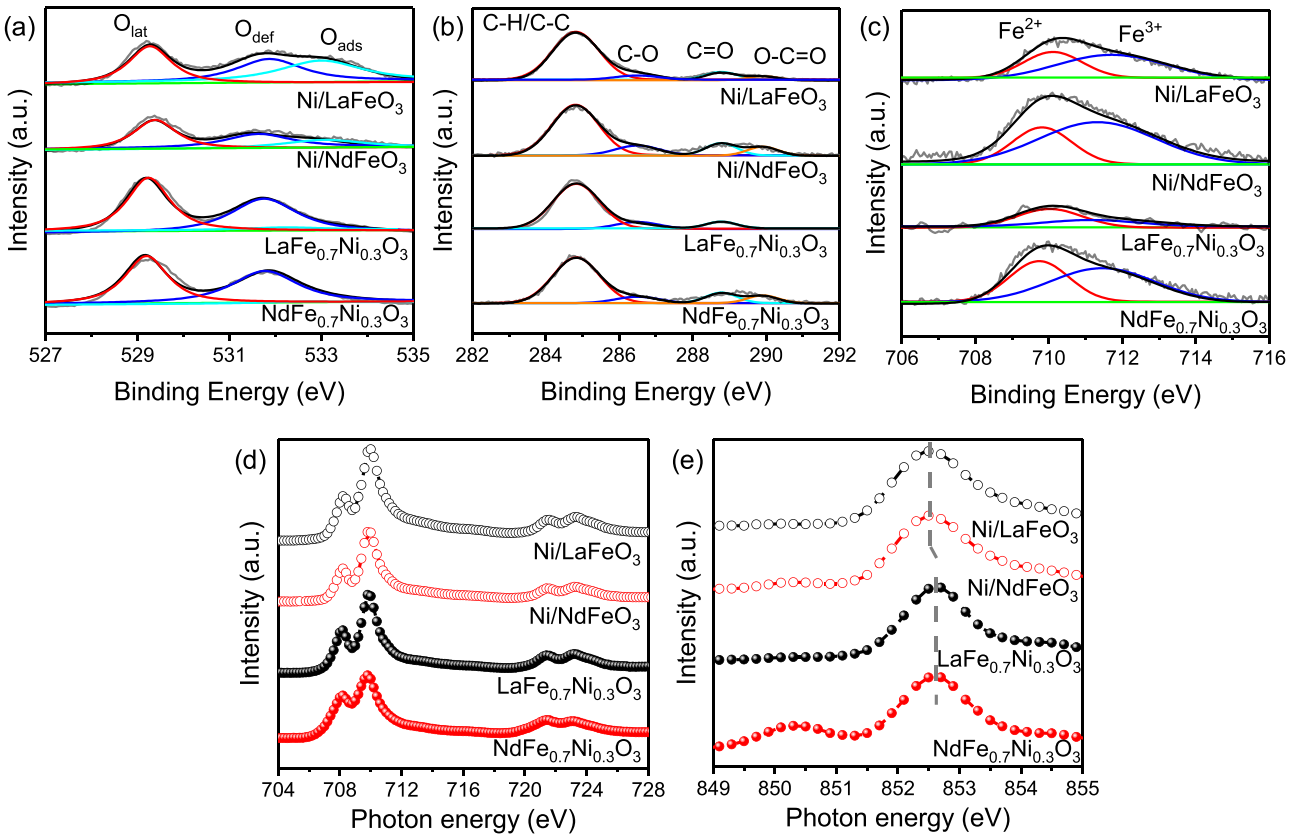

Fig. 8. XPS binding energies of spent catalysts: (a) O 1s region (b) C 1s region, (c) Fe $2p_{3/2}$ region; sXAS spectra of spent catalysts: (d) Fe $L_{3,2}$-edge and (e) Ni L_3-edge.

Table 2
XPS-derived characteristics for the spent catalysts.

Catalyst	Percentage of oxygen species (%)			O_{def}/O_{lat} ratio	Percentage of Fe irons (%)		Percentage of C species (%)			
	O_{lat}	O_{def}	O_{ads}		Fe^{2+}	Fe^{3+}	C-C/C-H	C-O	C=O	O-C=O
$Ni/LaFeO_3$	38.9	32.9	28.2	0.85	34.8	65.2	76.7	10.5	8.5	4.3
$Ni/NdFeO_3$	56.8	21.6	21.6	0.38	31.2	68.8	68.2	12.4	11.4	8.0
$LaFe_{0.7}Ni_{0.3}O_3$	50.6	46.3	3.1	0.92	67.0	33.0	84.4	7.3	8.3	-
$NdFe_{0.7}Ni_{0.3}O_3$	47.8	50.1	2.1	1.05	41.4	58.6	71.5	9.4	11.1	8.0

catalysts, which is noted in the later section. Arrhenius plots using the reaction rates of CO_2 and C_2H_6 over the catalysts are presented in Fig. S5 (c) and (d). The apparent activation barriers are measured at low C_2H_6 conversion (below 10 %) to minimize heat and mass transport limitations. Compared to $Ni/LnFeO_3$, Ni-doped $LnFe_{0.7}Ni_{0.3}O_3$ catalysts exhibit lower apparent activation barriers for both CO_2 and C_2H_6. $NdFe_{0.7}Ni_{0.3}O_3$ exhibits the lowest apparent activation energy, which matches its higher DRE activity.

3.3. Characterization of post-reaction catalysts

Through the EDX mapping of the spent catalysts in Fig. 4, it is shown that A-site elements and Fe are uniformly distributed in the perovskite. However, there exist obvious differences in the distribution of Ni on the catalysts. As shown in Fig. 4(a), green aggregated points are observed on the EDX mapping of Ni, representing that Ni species in $Ni/NdFeO_3$ are supported on $NdFeO_3$ as large nanoparticles, which is confirmed by the TEM images in Fig. S6. Meanwhile, it is found that the dispersion of Ni species is significantly enhanced through the doping-segregation process. Smaller nanoparticles are observed over the surface of spent $LaFe_{0.7}Ni_{0.3}O_3$ catalysts. As displayed in Fig. 4(c), with Nd^{3+} as the A-site cation, the dispersion of Ni is further improved, in which Ni species are homogeneously distributed on $NdFe_{0.7}Ni_{0.3}O_3$ after the DRE reaction. The higher dispersion of Ni over catalysts with Nd as an A-site cation might be due to the improvement of metal-support interaction and the inhibition of metal sintering [25,26].

In order to investigate the formation of carbon deposits during the reaction, the post-reaction catalysts were characterized by Raman spectroscopy and TGA. The amount of coke deposited on the catalysts after the reaction is determined by TGA and the results are shown in Fig. 5(a). For spent $Ni/NdFeO_3$ and $Ni/LaFeO_3$ catalysts, the weight loss is assigned to the oxidation of carbon deposits on the catalyst, corresponding to average coke formation rates of 0.116 and 0.054 g_{coke}/g_{cat} h^{-1}, respectively. For spent $LaFe_{0.7}Ni_{0.3}O_3$ and $NdFe_{0.7}Ni_{0.3}O_3$ catalysts, no weight loss is observed in this temperature range. The structure of the coke over the catalysts is determined by Raman spectroscopy. The Raman spectra of the spent $Ni/LaFeO_3$ and $Ni/NdFeO_3$ catalysts presented in Fig. 5(b) show two bands in the range of 1000–2000 cm^{-1}, which are associated with the D and G vibration modes of carbon materials. The so-called D band is related to disordered-induced Raman scattering from sp^2 carbons and the G band corresponds to the in plane bond-stretching motion of pairs of C sp^2 atoms. As a contrast, no Raman spectra of D band and G band are observed over spent $LaFe_{0.7}Ni_{0.3}O_3$ and $NdFe_{0.7}Ni_{0.3}O_3$ catalysts, indicating that $LaFe_{0.7}Ni_{0.3}O_3$ and

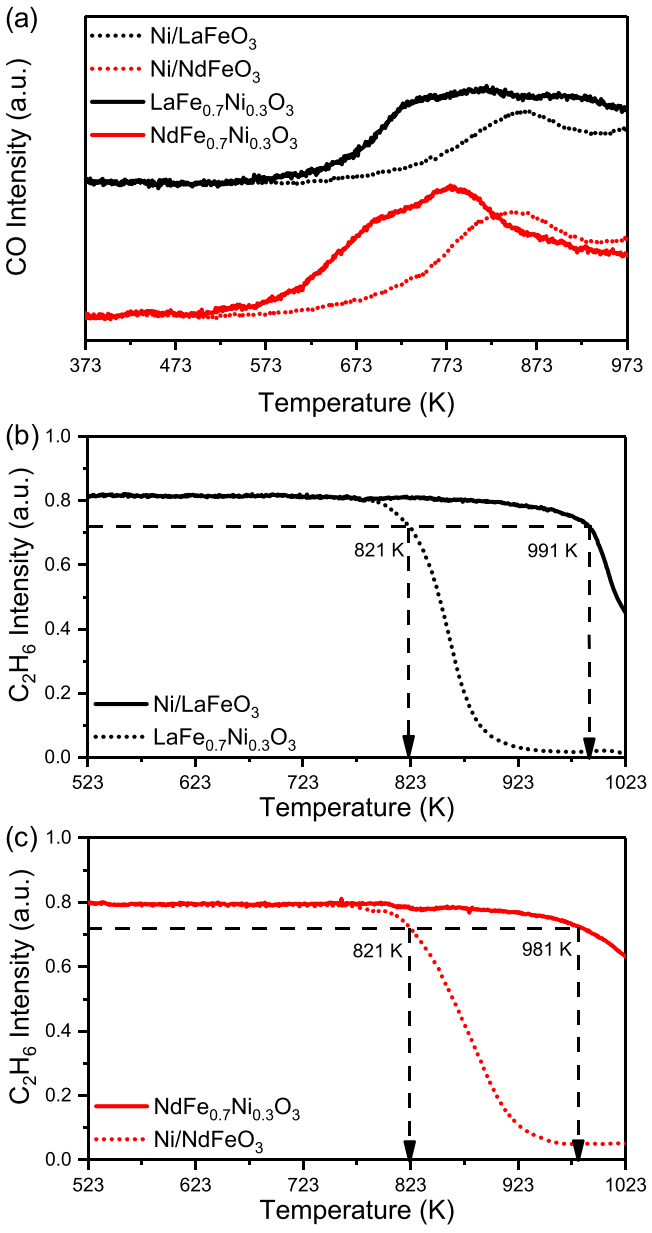

Fig. 9. TPSR profiles of catalysts: (a) CO_2-TPSR profiles of four catalysts; (b) C_2H_6-TPSR profiles of $Ni/LaFeO_3$ and $LaFe_{0.7}Ni_{0.3}O_3$; (c) C_2H_6-TPSR profiles of $Ni/NdFeO_3$ and $NdFe_{0.7}Ni_{0.3}O_3$.

$NdFe_{0.7}Ni_{0.3}O_3$ have strong resistance towards carbon deposition, which is in agreement with the TGA results.

In order to investigate the coke formation process on different catalysts, in-situ Raman experiments were carried out for $NdFe_{0.7}Ni_{0.3}O_3$ and $Ni/NdFeO_3$. As shown in Fig. 6(a), two Raman bands at 1330 cm^{-1} (D band) and 1600 cm^{-1} (G band) are detected over $NdFe_{0.7}Ni_{0.3}O_3$ with the introduction of C_2H_6/Ar, indicating the formation of coke on the surface of the catalyst. The coke maintains steady with the increasing reaction time and rapidly disappears after the switch of the inlet gas into CO_2/Ar. As a contrast, the higher intensity of D band and G band suggests more severe coke deposition on $Ni/NdFeO_3$. Not only the coke amount but also the nature of coke can be obtained through in-situ Raman. The carbon species formed on $Ni/NdFeO_3$ are just partially oxidized by CO_2/Ar and only O_2/Ar with stronger oxidation ability can fully oxidize them. According to the in-situ Raman results, it can be seen that $Ni/NdFeO_3$ and $NdFe_{0.7}Ni_{0.3}O_3$ show quite different coke formation processes. $NdFe_{0.7}Ni_{0.3}O_3$ shows much stronger resistance towards

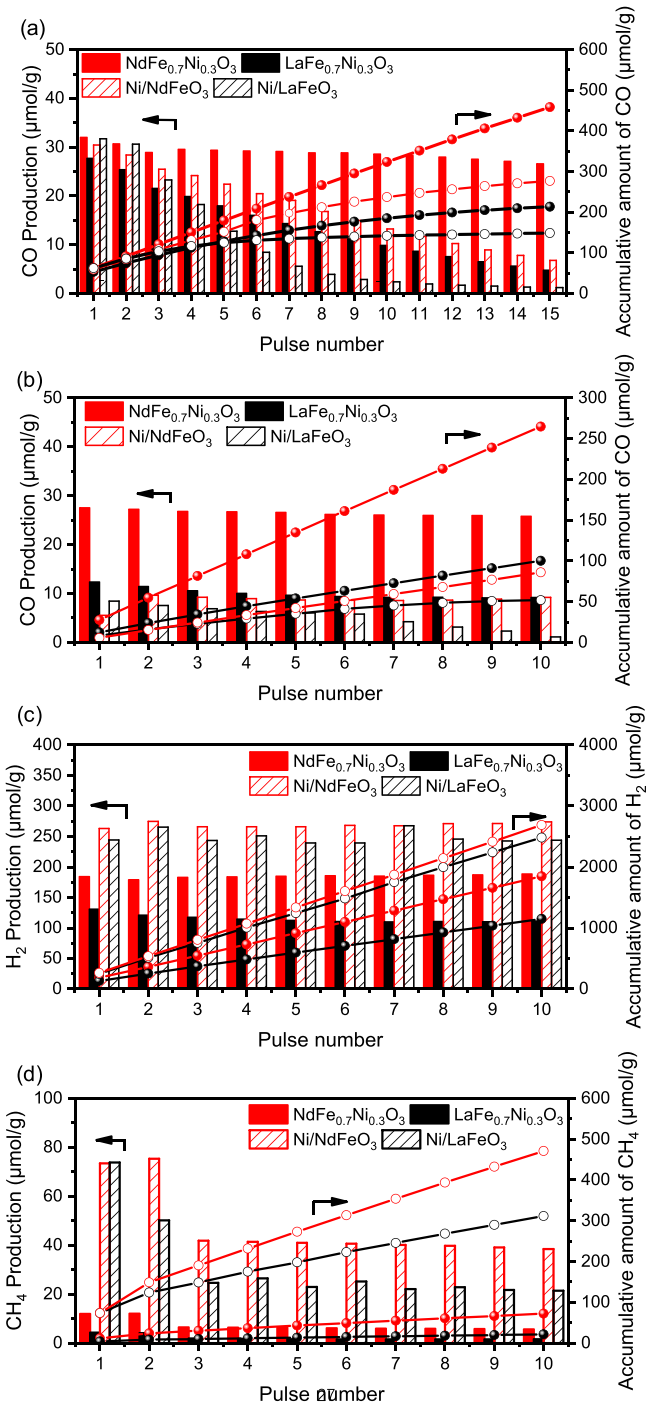

Fig. 10. Results of pulse reactions over $LaFe_{0.7}Ni_{0.3}O_3$, $NdFe_{0.7}Ni_{0.3}O_3$, $Ni/LaFeO_3$ and $Ni/NdFeO_3$: (a) CO production after the CO_2 pulse injections, (b) CO production after the C_2H_6 pulse injections in CO_2 - C_2H_6 pulse reaction, (c) H_2 production after the C_2H_6 pulse injections, (d) CH_4 production after the C_2H_6 pulse injections.

carbon deposition and faster coke elimination rates than those of $Ni/NdFeO_3$.

The electronic structure and local structure of the catalysts were determined by X-ray absorption near edge structure (XANES) and extended X-ray absorption fine structure (EXAFS) studies. The Ni K-edge XANES spectra of fresh catalysts are shown in Fig. 7(a), which are in good agreement with that of the NiO reference. The local coordination structure of Ni atoms was revealed by the phase-corrected Fourier transformation of EXAFS spectroscopy (FT-EXAFS). The Ni K-edge of

Table 3
Summary of the pulse reaction results.

Catalyst	CO (μmol/g)		H_2 (μmol/g)	CH_4 (μmol/g)	H_2:CH_4 ratio	H_2:CO ratio
	CO_2 pulse	C_2H_6 pulse				
$LaFe_{0.7}Ni_{0.3}O_3$	217	100	1148	22	52.2	11.5
$NdFe_{0.7}Ni_{0.3}O_3$	459	265	1845	72	25.6	7.0
$Ni/LaFeO_3$	149	52	2482	311	8.0	47.7
$Ni/NdFeO_3$	277	86	2687	471	5.7	31.2

pristine $NdFe_{0.7}Ni_{0.3}O_3$ and $LaFe_{0.7}Ni_{0.3}O_3$ shows just one main peak at ~1.65 Å in the R-space spectra in Fig. 7(b) without peaks of Ni-Ni bonding at ~2.18 Å, suggesting that Ni ions are highly dispersed in the lattice matrix of perovskites and the Ni-O species are isolated by A-site cations. After the DRE reaction, the white-line peak of Ni decreases dramatically and all the spent catalysts exhibit similar spectra as Ni foil in Fig. 7(c). The XAFS spectra of spent catalysts are shown in Fig. 7(d). The prominent peaks at 2.5 Å in the same position as that corresponding to Ni-Ni first coordination sphere in the metallic Ni used as a reference, showing a complete reduction to metallic Ni, which agrees with the above XANES results.

The surface elemental composition and chemical status of the catalysts were analyzed by the XPS technique. Fig. 8(a)–(c) show the O 1s, C 1s and Fe 2p spectra of the spent $Ni/LaFeO_3$, $Ni/NdFeO_3$, $LaFe_{0.7}Ni_{0.3}O_3$, and $NdFe_{0.7}Ni_{0.3}O_3$ catalysts. The atomic ratios of the surface species based on the corresponding fitted peaks are listed in Table 2. In the O 1s spectrum, three oxygen signals are observed at 533.8, 532.2, and 529.4 eV, which can be ascribed to hydroxyl and/or carbonate species on the surface (O_{ads}), dissociative oxygen on the oxygen defects (O_{def}), and lattice oxygen (O_{lat}), respectively [27,28]. Generally, the oxygen defect concentration over the perovskite catalysts is proportional to the O_{def}/O_{latt} ratio. The O_{def}/O_{lat} molar ratios over different catalysts exhibit the following sequence: $NdFe_{0.7}Ni_{0.3}O_3 > LaFe_{0.7}Ni_{0.3}O_3 > Ni/LaFeO_3 > Ni/NdFeO_3$. The relatively higher O_{def}/O_{lat} ratios over the $NdFe_{0.7}Ni_{0.3}O_3$ and $LaFe_{0.7}Ni_{0.3}O_3$ catalysts than the $Ni/LaFeO_3$ $Ni/NdFeO_3$ catalysts indicate that the exsolution of Ni ions from the perovskite promotes the formation of oxygen defects. The C 1s spectra of the spent catalysts are displayed in Fig. 8(b). The broad peak at 284.8 eV is corresponding to the absorbed carbon after exposure to ambient air or graphitic carbon. No signals of NiC_x were observed over all the catalysts. The peaks at higher binding energy indicate the formation of oxidized carbon species on the catalysts. In the Fe $2p_{3/2}$ spectrum, peaks at 712.5 and 709.0 eV are characteristic of Fe^{3+} and Fe^{2+} ions, respectively. The $NdFe_{0.7}Ni_{0.3}O_3$ and $LaFe_{0.7}Ni_{0.3}O_3$ catalysts exhibit obviously higher Fe^{2+}/Fe^{3+} ratio, suggesting that the incorporation of Ni into the perovskite improves the partial reduction of Fe ions.

In addition to XPS, soft XAS (sXAS) measurements were carried out to characterize the oxidation state of 3d metal atoms in the perovskite through monitoring 2p to 3d transitions in the L edges of 3d, which are surface sensitive and valence sensitive. The intensity ratio of the Fe-L_3 features at 708.1 and 708.7 eV in Fig. 8 (d) fingerprints the different Fe oxidation states. Consistent with the XPS results, the Ni-doped $LaFe_{0.7}Ni_{0.3}O_3$ and $NdFe_{0.7}Ni_{0.3}O_3$ catalysts exhibit higher Fe^{2+} ratios. The oxidation states of Ni are also determined by sXAS. As shown in Fig. 8(e), the shift of L_3 peak centroids of $LaFe_{0.7}Ni_{0.3}O_3$ and $NdFe_{0.7}Ni_{0.3}O_3$ catalysts to higher energy indicates a higher oxidation state of Ni [29], which originated from the electron transfer between Ni and the perovskite support.

DRIFTS measurements were performed to study the CO adsorption on catalysts and the normalized IR spectra of the adsorbed CO species on $NdFe_{0.7}Ni_{0.3}O_3$ and $Ni/NdFeO_3$ are displayed in Fig. S8. The adsorption spectrum of CO on $Ni/NdFeO_3$ exhibits one broad peak at 2001 cm^{-1}, which is assigned to linear-adsorbed CO species on Ni [30,31]. However, linear-adsorbed CO species observed on $NdFe_{0.7}Ni_{0.3}O_3$ is sharper, suggesting the enhanced uniformity of Ni dispersion, which is consistent with the EDX mapping results. In addition, the blue shift of linear Ni−CO bands on $NdFe_{0.7}Ni_{0.3}O_3$ demonstrates that the highly dispersed Ni species have a small number of 3d electronic states which weaken the Ni (3d)–CO($2\pi^*$) bonding through π back-donation, indicating more obvious charge transfer from the nickel to supports.

3.4. Activation of C_2H_6 and CO_2

The CO_2-TPSR studies were performed to probe the activation of CO_2 over the surface oxygen vacancies and the resulting spectra are presented in Fig. 9(a). The production of CO is attributed to the reaction between gas phase CO_2 and the oxygen vacancies in the catalysts to form CO and surface oxygen species. The oxygen vacancies are generated by the reduction/separation of Ni dopant atoms from the lattice of $NdFe_{0.7}Ni_{0.3}O_3$ and $LaFe_{0.7}Ni_{0.3}O_3$. The initial temperatures for CO_2 activation and CO formation follow the order of $NdFe_{0.7}Ni_{0.3}O_3 < LaFe_{0.7}Ni_{0.3}O_3 < Ni/NdFeO_3 \sim Ni/LaFeO_3$. The relatively lower activation temperature of $NdFe_{0.7}Ni_{0.3}O_3$ suggests the enhanced activity of CO_2 dissociation.

With the presence of surface oxygen species, the reactivity of C_2H_6 dissociation over the four catalysts was investigated by performing C_2H_6-TPSR experiments. Fig. 9(b) and (c) show the C_2H_6-TPSR profiles of $Ni/LaFeO_3$, $Ni/NdFeO_3$, $LaFe_{0.7}Ni_{0.3}O_3$ and $NdFe_{0.7}Ni_{0.3}O_3$ catalysts. The more active the metal is, the lower the dissociation temperature of C_2H_6 is observed. The temperature at which the conversion of ethane reaches 10 % is defined as T_{10}. T_{10} is 821 K for $Ni/LaFeO_3$ and Ni/

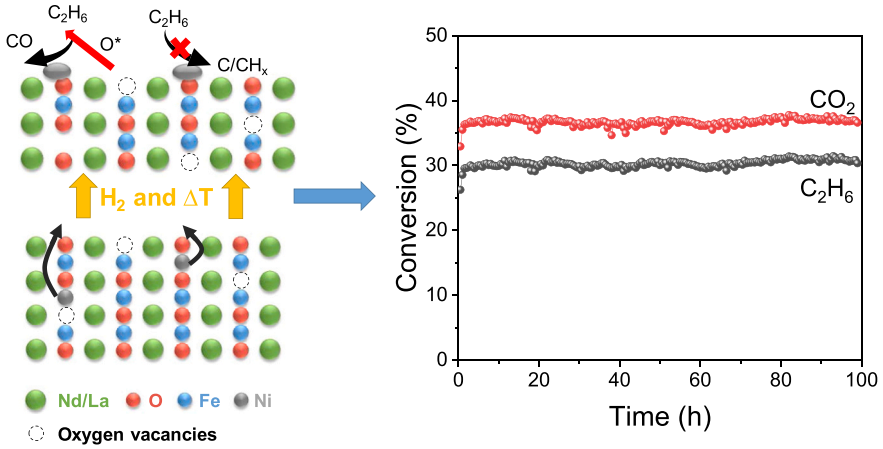

Fig. 11. Left: Mechanism diagram for the doping-segregation process and the activation of CO_2 and C_2H_6 over perovskite catalysts. Right: Conversion of the reactants over the $NdFe_{0.7}Ni_{0.3}O_3$ catalyst at 873 K for 100 h reaction.

$NdFeO_3$ while it increases to 981 K and 991 K for $NdFe_{0.7}Ni_{0.3}O_3$, and $LaFe_{0.7}Ni_{0.3}O_3$, respectively. The results indicate that the direct dissociation of C_2H_6 is suppressed over $NdFe_{0.7}Ni_{0.3}O_3$ and $LaFe_{0.7}Ni_{0.3}O_3$ with the assistance of surface oxygen species. Compared to $LaFe_{0.7}Ni_{0.3}O_3$, Ni/$LaFeO_3$, and Ni/$NdFeO_3$, $NdFe_{0.7}Ni_{0.3}O_3$ shows moderate activity for C_2H_6 activation therefore $NdFe_{0.7}Ni_{0.3}O_3$ achieves a combination of high catalytic activity and coke resistance.

To confirm the results of TPSR, the step response reactions were also carried out over the catalysts at 873 K. Fig. S9 shows transient response curves of H_2 and CH_4 obtained during C_2H_6 steps over the catalysts. When the feed gas is switched from Ar to C_2H_6, it is seen that differently shaped H_2 and CH_4 transient response curves appear. As displayed in Fig. S9(a), only a small amount of H_2 production is observed on $LaFe_{0.7}Ni_{0.3}O_3$, illustrating the poor activity towards the dissociation of C_2H_6. On the contrary, a significant increase in the amount of H_2 production accompanied with the production of a large amount of CH_4 is found on Ni/$NdFeO_3$ in Fig. S9(b). The imbalance between the high activity for C_2H_6 dissociation and the poor activity for CO_2 activation leads to severe coke deposition. Consistent with C_2H_6-TPSR results, $NdFe_{0.7}Ni_{0.3}O_3$ exhibits a proper C_2H_6 activation rate and thus the coke formation through C_2H_6 dissociation could be efficiently eliminated by the surface oxygen species.

Pulse reactions were employed to quantitatively investigate the products of CO_2 activation and C_2H_6 activation with the assistance of surface oxygen species. From the chemical stoichiometry, the production of CO during the CO_2 pulses should be equal to the number of oxygen vacancies or mobile oxygen atoms. The accumulative CO formation amount represents the consumption amount of the surface oxygen vacancies, which is calculated to be 459 and 217 μmol/g on $NdFe_{0.7}Ni_{0.3}O_3$ and $LaFe_{0.7}Ni_{0.3}O_3$, respectively. As a comparison, the total amounts of oxygen vacancies on the reduced Ni/$NdFeO_3$ and Ni/$LaFeO_3$ catalysts are only 277 and 149 μmol/g, respectively. These atoms can participate in the oxidation of surface carbon deposits, playing a significant role in the elimination of coke deposition. Moreover, the accumulated CO amount produced in ethane pulses of CO_2 - C_2H_6 pulse reactions is a critical parameter to reflect the oxygen supply capacity. According to Fig. 10(b) and Table 3, it is concluded that $NdFe_{0.7}Ni_{0.3}O_3$ gains more oxygen from CO_2 and provides more oxygen participating in the activation of C_2H_6 and the oxidation of surface carbon deposits. The product distribution for C_2H_6 activation was also determined by C_2H_6 pulse reactions. As shown in Fig. 10(c) and (d) and Table 3, although $NdFe_{0.7}Ni_{0.3}O_3$ and $LaFe_{0.7}Ni_{0.3}O_3$ exhibit lower H_2 production, more fraction of C_2H_6 is converted into CO rather than CH_4 and surface carbon with the assistance of mobile oxygen. The increase in the amount of mobile oxygen and decrease in the activity for C_2H_6 direct dissociation leads to stronger resistance to coke accumulation.

3.5. Mechanistic insights into the effect of A-site cations

In this work, the poor stability of impregnated Ni/$NdFeO_3$ and Ni/$LaFeO_3$ catalysts is due to the deactivation caused by carbon deposition according to the TGA and Raman results. In-situ Raman reveals that $NdFe_{0.7}Ni_{0.3}O_3$ shows stronger resistance towards carbon accumulation and the carbon species formed on the surface of $NdFe_{0.7}Ni_{0.3}O_3$ is more likely to be oxidized.

According to the mechanism for the dry reforming of light-alkanes reported in previous literature, it is widely acknowledged that the metal-support synergistic effect may strongly affect the activity and coking resistance of the catalysts. Such a synergistic effect describes that alkane is activated on the metal sites while CO_2 is activated on the oxide support. The XANES, XAFS, and in-situ XRD data show the high dispersion of doping Ni in the perovskite lattice and the complete expulsion of Ni from the lattice under a reductive atmosphere. The CO_2-TPSR and pulse reaction results reveal that oxygen vacancies generated by the exsolution of Ni from the perovskite provide active sites for the dissociation of CO_2 and promote the removal of deposited carbon species. XAS, XPS, and H_2-TPR experiments demonstrate that the Ni species is positively charged through the doping-segregation process. According to the results of C_2H_6-TPSR, step response, and pulse reaction studies, the positively charged nickel ($Ni^{\delta+}$) inhibits the direct dissociation of ethane into surface carbon species, leading to a positive effect on coke suppression.

Thus, we conclude that the A-site cation and the doping-segregation process of the perovskite catalysts affect their catalytic activity and stability for the DRE reaction. As shown in Fig. 11, compared with $LaFe_{0.7}Ni_{0.3}O_3$, Ni/$NdFeO_3$, and Ni/$LaFeO_3$, $NdFe_{0.7}Ni_{0.3}O_3$ with higher oxygen storage capacity generates more mobile active oxygen species that promote both the partial oxidation of C_2H_6 and the removal of deposited carbon species. Moreover, $NdFe_{0.7}Ni_{0.3}O_3$ exhibits a proper C_2H_6 activation rate with a higher Ni dispersion and stronger metal-support interaction. In addition, ethane is activated with the assistance of surface oxygen species over $NdFe_{0.7}Ni_{0.3}O_3$ instead of being directly dissociated into surface carbon. As a consequence, the balance between the rate of carbon generation and the rate of carbon consumption can be achieved for dry reforming of ethane over $NdFe_{0.7}Ni_{0.3}O_3$, leading to a coke-free reaction mechanism and thereafter an improved overall catalytic performance.

4. Conclusion

Single-phase perovskite catalysts ($LnFe_{0.7}Ni_{0.3}O_3$) with different rare earth A site cations were successfully synthesized using a sol-gel method and evaluated as catalyst precursors in the DRE reaction with Ni/$LnFeO_3$ catalysts as the references. The DRE activity follows the trend: $NdFe_{0.7}Ni_{0.3}O_3$ > $SmFe_{0.7}Ni_{0.3}O_3$ > $EuFe_{0.7}Ni_{0.3}O_3$ > $LaFe_{0.7}Ni_{0.3}O_3$. $NdFe_{0.7}Ni_{0.3}O_3$ shows high conversion of C_2H_6 and CO_2, excellent syngas selectivity, and robust maintenance of the performance with no coke formation over 100 h reaction. In contrast with Ni/$LnFeO_3$, $LnFe_{0.7}Ni_{0.3}O_3$ provides more oxygen vacancies through the doping-segregation process to activate CO_2 and generate surface oxygen species. The surface oxygen atoms facilitate the conversion of C_2H_6 into CO rather than into surface carbon and promote the oxidation of surface carbon deposits on the catalyst. The doping-segregation method also modifies the metal-support interaction and the electronic properties of Ni. The positively charged nickel ($Ni^{\delta+}$) suppresses the direct dissociation of C_2H_6 into surface carbon, leading to a coke-free reaction mechanism. In summary, this study clearly establishes that $NdFe_{0.7}Ni_{0.3}O_3$ is a highly coke-resistant catalyst with immense potential for commercial exploitation and also sheds new light on tuning the catalytic performance for different reactions through substituting A-site cations and applying the doping-segregation method.

CRediT authorship contribution statement

Yaning Wang: Investigation, Methodology, Conceptualization, Writing – review & editing, Visualization. **Xiaohang Sun:** Investigation, Validation. **Xiaohan Yu:** Investigation, Writing – original draft. **Rongjun Zhang**: Resources, Project administration. **Binhang Yan:** Conceptualization, Supervision, Writing – review & editing, Funding acquisition.

Declaration of Competing Interest

The authors declare that they have no known competing financial interests or personal relationships that could have appeared to influence the work reported in this paper.

Data Availability

The data that has been used is confidential.

Acknowledgments

This work was supported by the National Natural Science Foundation of China (NSFC, Grant No. 21978148). The authors thank beamline 4B9A and beamline 4B9B at the Beijing Synchrotron Radiation Facility (BSRF) for providing the beam time.

Appendix A. Supporting information

Supplementary data associated with this article can be found in the online version at doi:10.1016/j.apcatb.2023.123010.

References

[1] H.L. Chen, H.M. Lee, S.H. Chen, Y. Chao, M.B. Chang, Review of plasma catalysis on hydrocarbon reforming for hydrogen production—interaction, integration, and prospects, Appl. Catal. B: Environ. 85 (2008) 1–9.
[2] Z. Li, M. Li, Z. Bian, Y. Kathiraser, S. Kawi, Design of highly stable and selective core/yolk–shell nanocatalysts—a review, Appl. Catal. B: Environ. 188 (2016) 324–341.
[3] T.-L. Hsieh, Y. Zhang, D. Xu, C. Wang, M. Pickarts, C. Chung, L.-S. Fan, A. Tong, Chemical looping gasification for producing high purity, H2-rich syngas in a cocurrent moving bed reducer with coal and methane cofeeds, Ind. Eng. Chem. Res. 57 (2018) 2461–2475.
[4] B. Lee, H.-S. Cho, H. Kim, D. Lim, W. Cho, C.-H. Kim, H. Lim, Integrative techno-economic and environmental assessment for green H2 production by alkaline water electrolysis based on experimental data, J. Environ. Chem. Eng. 9 (2021), 106349.
[5] S.M. Kim, P.M. Abdala, T. Margossian, D. Hosseini, L. Foppa, A. Armutlulu, W. van Beek, A. Comas-Vives, C. Copéret, C. Müller, Cooperativity and dynamics increase the performance of NiFe dry reforming catalysts, J. Am. Chem. Soc. 139 (2017) 1937–1949.
[6] G.A. Olah, A. Goeppert, M. Czaun, G.K.S. Prakash, Bi-reforming of methane from any source with steam and carbon dioxide exclusively to metgas (CO–2H2) for methanol and hydrocarbon synthesis, J. Am. Chem. Soc. 135 (2013) 648–650.
[7] G.A. Olah, A. Goeppert, M. Czaun, T. Mathew, R.B. May, G.K.S. Prakash, Single step Bi-reforming and oxidative Bi-reforming of Methane (Natural Gas) with steam and carbon dioxide to metgas (CO-2H2) for methanol synthesis: self-sufficient effective and exclusive oxygenation of methane to methanol with oxygen, J. Am. Chem. Soc. 137 (2015) 8720–8729.
[8] R.K. Singha, A. Yadav, A. Agrawal, A. Shukla, S. Adak, T. Sasaki, R. Bal, Synthesis of highly coke resistant Ni nanoparticles supported MgO/ZnO catalyst for reforming of methane with carbon dioxide, Appl. Catal. B: Environ. 191 (2016) 165–178.
[9] M. Muraleedharan Nair, S. Kaliaguine, Structured catalysts for dry reforming of methane, New J. Chem. 40 (2016) 4049–4060.
[10] S. Singh, D. Zubenko, B.A. Rosen, Influence of LaNiO3 shape on its solid-phase crystallization into coke-free reforming catalysts, ACS Catal. 6 (2016) 4199–4205.
[11] B. Zhao, R. Ran, L. Sun, X. Guo, X. Wu, D. Weng, NO catalytic oxidation over an ultra-large surface area LaMnO3+δ perovskite synthesized by an acid-etching method, RSC Adv. 6 (2016) 69855–69860.
[12] A.G. Bhavani, W.Y. Kim, J.S. Lee, Barium substituted lanthanum manganite perovskite for CO_2 reforming of methane, ACS Catal. 3 (2013) 1537–1544.
[13] Y. Nishihata, J. Mizuki, T. Akao, H. Tanaka, M. Uenishi, M. Kimura, T. Okamoto, N. Hamada, Self-regeneration of a Pd-perovskite catalyst for automotive emissions control, Nature 418 (2002) 164–167.
[14] D. Neagu, T.-S. Oh, D.N. Miller, H. Ménard, S.M. Bukhari, S.R. Gamble, R.J. Gorte, J.M. Vohs, J.T.S. Irvine, Nano-socketed nickel particles with enhanced coking resistance grown in situ by redox exsolution, Nat. Commun. 6 (2015) 8120.
[15] P. Steiger, M. Nachtegaal, O. Kröcher, D. Ferri, Reversible segregation of Ni in LaFe 0.8 Ni 0.2 O 3± δ during coke removal, ChemCatChem 10 (2018) 4456–4464.
[16] J.L.G. Fierro, Structure and composition of perovskite surface in relation to adsorption and catalytic properties, Catal. Today 8 (1990) 153–174.
[17] J. Deng, M. Cai, W. Sun, X. Liao, W. Chu, X.S. Zhao, Oxidative methane reforming with an intelligent catalyst: sintering-tolerant supported nickel nanoparticles, ChemSusChem 6 (2013) 2061–2065.
[18] B. Zhao, B. Yan, S. Yao, Z. Xie, Q. Wu, R. Ran, D. Weng, C. Zhang, J.G. Chen, LaFe0.9Ni0.1O3 perovskite catalyst with enhanced activity and coke-resistance for dry reforming of ethane, J. Catal. 358 (2018) 168–178.
[19] S. Keav, S.K. Matam, D. Ferri, A. Weidenkaff, Structured perovskite-based catalysts and their application as three-way catalytic converters-a review, Catalysts 4 (2014) 226–255.
[20] G.R. Moradi, M. Rahmanzadeh, The influence of partial substitution of alkaline earth with La in the LaNiO3 perovskite catalyst, Catal. Commun. 26 (2012) 169–172.
[21] S.O. Choi, S.H. Moon, Performance of La1−xCexFe0.7Ni0.3O3 perovskite catalysts for methane steam reforming, Catal. Today 146 (2009) 148–153.
[22] M. Wang, T. Zhao, X. Dong, M. Li, H. Wang, Effects of Ce substitution at the A-site of LaNi0.5Fe0.5O3 perovskite on the enhanced catalytic activity for dry reforming of methane, Appl. Catal. B: Environ. 224 (2018) 214–221.
[23] L. Zhao, T. Han, H. Wang, L. Zhang, Y. Liu, Ni-Co alloy catalyst from LaNi1−xCoxO3 perovskite supported on zirconia for steam reforming of ethanol, Appl. Catal. B: Environ. 187 (2016) 19–29.
[24] Z. Xie, B. Yan, J.H. Lee, Q. Wu, X. Li, B. Zhao, D. Su, L. Zhang, J.G. Chen, Effects of oxide supports on the CO_2 reforming of ethane over Pt-Ni bimetallic catalysts, Appl. Catal. B: Environ. 245 (2019) 376–388.
[25] Q. Wang, G. Li, B. Zhao, R. Zhou, The effect of Nd on the properties of ceria–zirconia solid solution and the catalytic performance of its supported Pd-only three-way catalyst for gasoline engine exhaust reduction, J. Hazard. Mater. 189 (2011) 150–157.
[26] R. Zhang, F. Li, N. Zhang, Q. Shi, Benzene hydrogenation over amorphous NiB/bentonite catalyst and promoting effect of Nd, Appl. Catal. A: Gen. 239 (2003) 17–23.
[27] W. Xingyi, K. Qian, L. Dao, Catalytic combustion of chlorobenzene over MnOx–CeO2 mixed oxide catalysts, Appl. Catal. B: Environ. 86 (2009) 166–175.
[28] Z. Wei, M. Zhao, Z. Yang, X. Duan, G. Jiang, G. Li, F. Zhang, Z. Hao, Oxygen vacancy-engineered titanium-based perovskite for boosting H(2)O activation and lower-temperature hydrolysis of organic sulfur, Proc. Natl. Acad. Sci. USA 120 (2023), e2217148120.
[29] W. Gu, H. Wang, K. Wang, Nickel L-edge and K-edge X-ray absorption spectroscopy of non-innocent Ni[S2C2(CF3)2]2n series (n = −2, −1, 0): direct probe of nickel fractional oxidation state changes, Dalton Trans. 43 (2014) 6406–6413.
[30] C. Vogt, E. Groeneveld, G. Kamsma, M. Nachtegaal, L. Lu, C.J. Kiely, P.H. Berben, F. Meirer, B.M. Weckhuysen, Unravelling structure sensitivity in CO_2 hydrogenation over nickel, Nat. Catal. 1 (2018) 127–134.
[31] T.S. Galhardo, A.H. Braga, B.H. Arpini, J. Szanyi, R.V. Goncalves, B.F. Zornio, C. R. Miranda, L.M. Rossi, Optimizing active sites for high CO selectivity during CO_2 hydrogenation over supported nickel catalysts, J. Am. Chem. Soc. 143 (2021) 4268–4280.